Research Paper

Mid- to late-Holocene sea-level evolution of the northeastern Aegean sea

Martin Seeliger,[1] Anna Pint,[2] Peter Frenzel,[2] Nick Marriner,[3]
Giorgio Spada,[4] Matteo Vacchi,[5] Sait Başaran,[6] Anca Dan,[7]
Friederike Seeger,[8] Katharina Seeger,[9] Thomas Schmidts[10]
and Helmut Brückner[9]

Abstract

We combined biostratigraphical analyses, archaeological surveys, and Glacial Isostatic Adjustment (GIA) models to provide new insights into the relative sea-level evolution in the northeastern Aegean Sea (eastern Mediterranean). In this area, characterized by a very complex tectonic pattern, we produced a new typology of sea-level index point, based on the foraminiferal associations found in transgressive marine facies. Our results agree with the sea-level history previously produced in this region, therefore confirming the validity of this new type of index point. The expanded dataset presented in this paper further demonstrates a continuous Holocene RSL rise in this portion of the Aegean Sea. Comparing the new RSL record with the available geophysical predictions of sea-level evolution indicates that the crustal subsidence of the Samothraki Plateau and the North Aegean Trough played a major role in controlling millennial-scale sea-level evolution in the area. This major subsidence rate needs to be taken into account in the preparation of local future scenarios of sea-level rise in the coming decades.

Highlights

- Relative sea level in the Northern Aegean region is today at its Holocene peak
- Assemblage of benthic foraminifers established as a valid sea-level index point
- Field-based data challenge existing GIA models
- Archeological sea-level limiting points help to clarify the sea-level evolution

Introduction

A number of factors drive sea-level changes (eustatic, isostatic, steric and geotectonic factors, sediment supply, coastal dynamics, and sediment compaction) at diverse spatial and temporal timescales (Benjamin et al., 2017; Khan et al., 2017; Lambeck and Purcell, 2005; Shennan et al., 2018). This is especially true for the region of the Meriç delta on the border between Greece and Turkey. Together with the Nestos, Kompsatos, and Lissos rivers, the Meriç (Evros, Maritsa; ancient name: Hebros) constitutes one of the largest sources of fresh water and sediment load to the northern Aegean Sea (Poulos and Kotinas, 2020; Sakellariou and Galanidou, 2015; Uckac et al., 2006; Figures 1 and 2).[1]

Like the adjacent Samothraki Plateau – a very shallow portion of the Northern Aegean with a bathymetry <100 m and extending between the islands of Thasos and Samothraki and the Enez region – the Meriç delta has been significantly affected by sea-level fluctuations during the Quaternary (Sakellariou and Galanidou, 2015; Theocharis and Georgopoulos, 1993). The Samothraki Plateau was dry, presenting a near-coastal dune landscape during

most of the Quaternary glacial periods and, in particular, at the end of the Last Glacial Maximum (LGM, around 21 ka BP), when sea level was at least 120 m below the present datum (Lambeck and Purcell, 2005; Papoulia, 2017).

This paper provides new insights into the area's Relative Sea-Level (RSL) history, where just a few studies have been conducted so far. In particular, the hypothesis of an isostatic-driven mid-Holocene sea-level highstand between 6000 and 3500 cal yrs BP that

[1]Department of Physical Geography, Faculty of Geosciences, Goethe University Frankfurt, Frankfurt, Germany
[2]Institute of Geosciences, Friedrich Schiller University Jena, Jena, Germany
[3]CNRS, ThéMA, Universite de Franche-Comte, UMR 6049, MSHE Ledoux, Besançon, France
[4]Dipartimento di Fisica e Astronomia, Università di Bologna, Bologna, Italy
[5]Dipartimento di Scienze della Terra, Università di Pisa, Pisa, Italy
[6]Edebiyat Fakültesi, İstanbul Üniversitesi, Beyazıt, Fatih/İstanbul, Turkey
[7]CNRS, AOrOc, École normale supérieure, Paris, France
[8]Institute of Geography, Heidelberg University, Heidelberg, Germany
[9]Institute of Geography, University of Cologne, Cologne, Germany
[10]Römisch-Germanisches Zentralmuseum, Leibniz-Forschungsinstitut für Archäologie, Mainz, Germany

Corresponding author:
Martin Seeliger, Department of Physical Geography, Faculty of Geosciences, Goethe University Frankfurt, Altenhöferallee 1, 60438 Frankfurt, Germany.
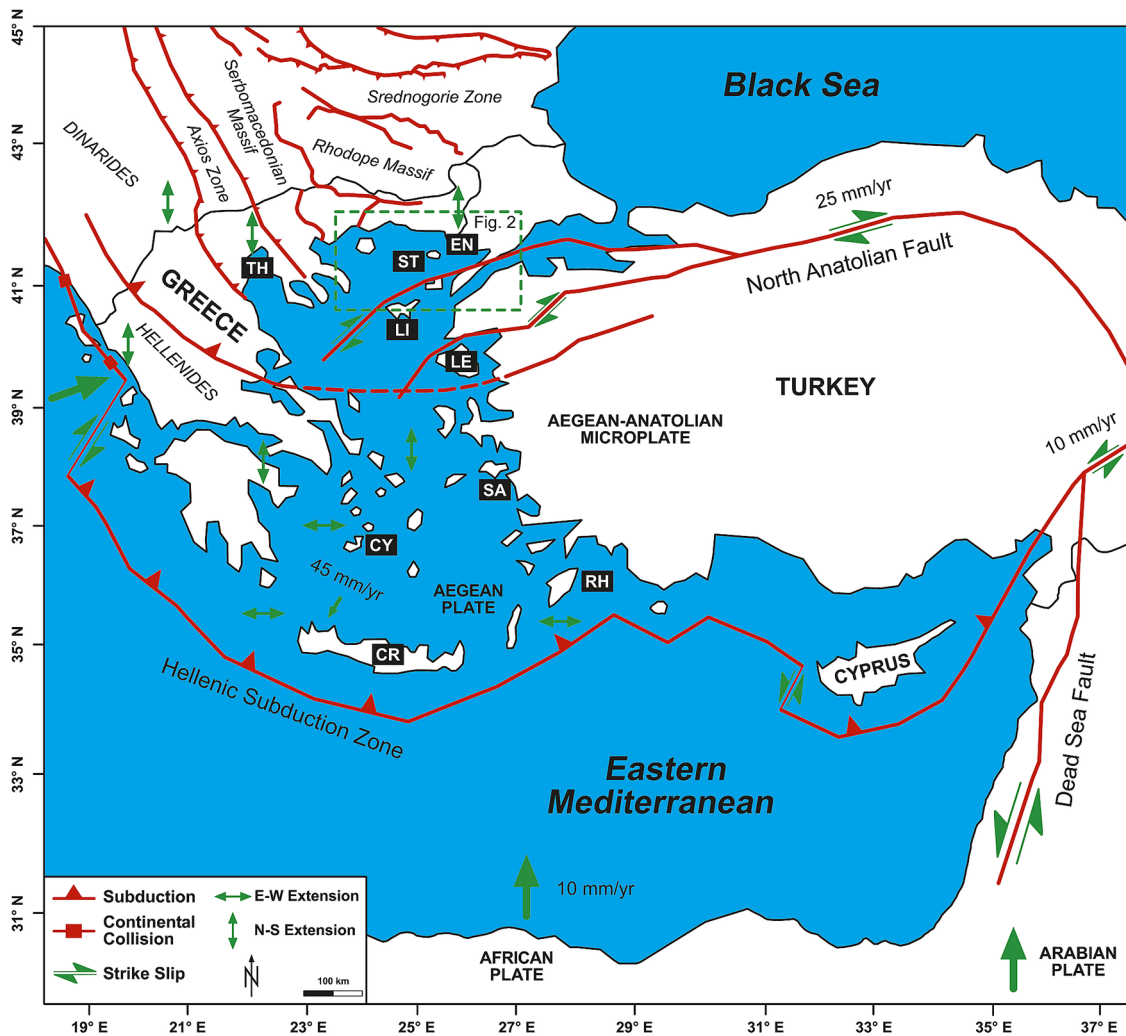Email: seeliger@em.uni-frankfurt.de

Figure 1. Tectonic overview of the Aegean Region.
Several sites presented in this study are marked: TH: Thessaloniki; ST: Samothraki; EN: Enez; LI: Limnos; LE: Lesvos; SA: Samos; RH: Rhodes; CR: Crete; CY: Cyclades. Based on Maravelis et al. (2015).

exceeded present mean sea level (Brückner et al., 2006; Kayan, 1988; Kraft et al., 1980) was recently confuted by the production of new RSL data (Vacchi et al., 2014). These new analyses indicate a continuous rise of the RSL in the North Aegean throughout the Holocene period. However, the different mechanisms, which controlled sea-level evolution in recent millennia in this portion of the Aegean, are poorly constrained. To fill this knowledge gap, the results of geoarcheological (Brückner et al., 2015) and geophysical (Schwardt et al., 2020; Seeliger et al., 2018) studies offer possibilities to produce new relative sea-level data and furnish fresh perspectives on its evolution.

While reconstructing the coastal evolution of the ancient harbor city of Elaia (Feuser et al., 2018; Seeliger et al., 2019), the maritime satellite of Pergamon (today Bergama/Turkey), Seeliger et al. (2017) established an RSL curve for the area by presenting a new sea-level indicator, based on Holocene foraminiferal successions. The reconstructed RSL curve meshes well with results from studies of adjacent Aegean regions (Seeliger et al., 2017) and shows – in accordance with Vacchi et al. (2014) – that RSL has never been higher than present during the Holocene.

To investigate the relative sea-level evolution in a different area of the Aegean, this study aims to: (I) validate this "new" sea-level indicator in a different area of the Aegean; (II) establish a regional RSL curve; and (III) compare and contrast this curve with other field-based RSL data and modeled geophysical data based on available Glacial Isostatic Adjustment (GIA) models for the Aegean region.

Geographical and geological setting

The study area – around the city of Enez (ancient Ainos) – is located in the westernmost part of Turkish Thrace (Figures 1 and 2), in direct vicinity to the river mouth of the Meriç.

In general, the Nothern Aegean region's geotectonic setting is triggered by the northward drift of the Arabian microplate that pushes the Aegean-Anatolian microplate westwards along the dextral strike-slip North Anatolian Fault (NAF; Figure 1). As a westward prolongation of the NAF into the Aegean Sea acts the North Aegean Trough (NAT), which comprises a series of deep basins developed due to transtension along the westernmost parts of the NAF reaching water depths of 1000 m (Figure 2). The NAT is the border between the relatively non-deforming but, roughly speaking, subsiding North Aegean Shelf region, including the shallow Samothraki Plateau from the deforming Aegean to its south. The North Aegean shores south of the Rhodope Massif generally show long-term subsidence. However, due to its fragmentation into different orogenetic blocks (Figure 1), the subsidence rates are not uniform between Thessaloniki and Enez (Galanidou et al., 2020; Jackson, 1994). In contrast, fault-bounded crustal blocks, such as the islands of Samothraki and Thasos and the Peninsula of Chalkidiki, act differently from this regional trend. They show tectonic uplift attested by human settlements of Pleistocene age on Thasos and at Chalkidiki (Figures 1 and 2; Armijo et al., 1999; Brückner et al., 2015; Maravelis et al., 2015; Sakellariou and Galanidou, 2015).
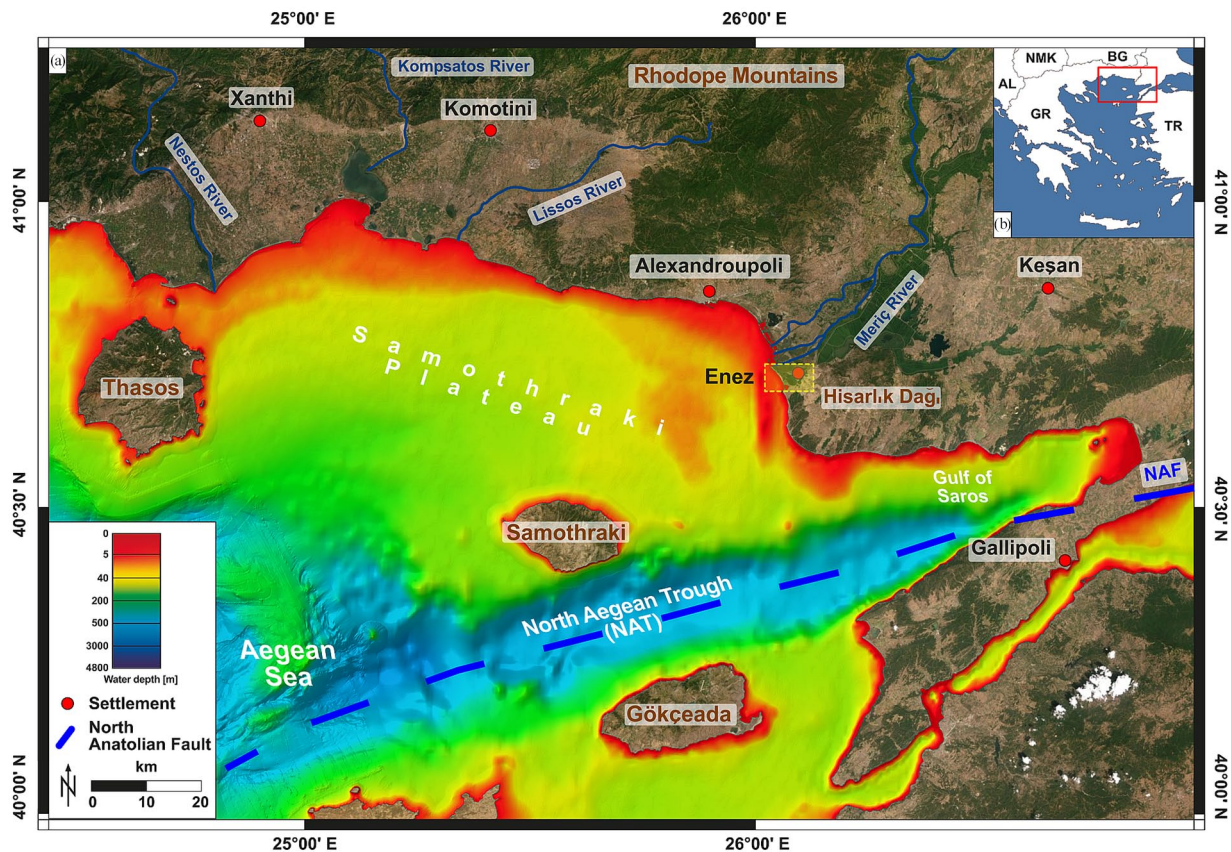
Figure 2. Research area in the northern Aegean between the Island of Thasos and the Gulf of Saros. (a) Overview map with locations mentioned in the text and the four major rivers of the region (Nestos, Kompsatos, Lissos, and Meriç), which have their sources in the Rhodope Mountains and deposit their high sediment load on the shallow shelf of the Samothraki Plateau. (b) Position of Figure 2a on a general map of the Aegean Sea and its bordering countries.
The map was created using QGIS software. For the land cover, the standard basemap of QGIS is used. The bathymetry is based on the open dataset "Bathymetry – Understanding the topography of the European seas," provided by the EMODnet Bathymetry Consortium (2018) of the European Union (https://portal.emodnet-bathymetry.eu; accessed: 17th July 2020).
GR: Greece; AL: Albania; NMK: North Macedonia; BG: Bulgaria; TR: Turkey.

The Meriç debouches into the Aegean Sea by creating an extensive deltaic floodplain of 180 km^2 between the Greek city of Alexandroupoli and the Turkish city of Enez (Figures 2 and 3; Barut et al., 2015). The Holocene evolution of the Meriç delta is complex and unclear at present. This knowledge gap is compounded by the delta's position on the border between Turkey and Greece, which renders transboundary investigations challenging. Due to the delta's complexity, the use of the sea-level indicator established by Seeliger et al. (2017) is particularly suitable, thanks notably to the stable bedrock of the castle hill of Ainos. Immediately in front of the Meriç River mouth, the Samothraki Plateau extends between the islands of Thasos and Samothraki with water depths <100 m. The entire region is fed with fresh water and sediments from the Nestos, Kompsatos, Lissos, and Meriç rivers, all sourced in the Rhodope Mountains, north of the Greek cities Xanthi, Komotini, and Alexandroupoli (Poulos and Kotinas, 2020; Saltogianni et al., 2016; Figures 1 and 2).

Materials and methods

Between 2011 and 2017, sediment cores were taken to reconstruct the palaeoenvironmental evolution of the area close to the Meriç river mouth. This study includes the data of three of them (Ain 6, 115, and 123; Figure 3). These cores hit bedrock, topped by the marine transgression, and are used for relative sea-level reconstructions based on the indicator described by Seeliger et al. (2017). (Brückner et al., 2015; Pint et al., 2015; Rabbel et al., 2015; Schwardt et al., 2020; Seeliger et al., 2018).

Fieldwork and geodesy

Coring was performed using an *Atlas Copco Cobra TT* vibracorer. Open steel auger heads (outer diameters: 6 and 5 cm, respectively) were used to probe the stratigraphy. In the field, the cores were sampled at constant intervals (10–15 cm). DGPS leveling (<2 cm resolution) was performed using a *Topcon HIPER Pro* device. The local coordinate system (LCS) applied in Enez and used in this study is based on UTM (zone 35N) using WGS84. Ellipsoidal heights were transformed to orthometric ones by applying the geoid model EGG97. The altitude correction of the LCS is undergirded according to the ITRF08 standard by processing the data with the web service of the *Geodetic Survey Division, Canada Centre for Remote Sensing, Natural Resources Canada*. Our sea-level measurements by DGPS, during fieldwork in 2013–2015, supported the LCS sea-level heights. Furthermore, these DGPS measurements revealed a micro-tidal regime (tidal range: approx. 20 cm), common for the Aegean Sea (Seeliger et al., 2019; Vacchi et al., 2012). All elevations are stated in m b.s. (meters below the surface), m a.s.l. (meters above present-day mean sea level) or m b.s.l. (meters below present-day mean sea level).

Laboratory analyses

Grain-size analyses were conducted on the retrieved sediment samples (Bartz et al., 2017; Ernst, 1970; Ginau et al., 2018). Samples were air-dried, ground with a mortar and pestle, and sieved to separate the ≤2 mm grain-size fraction for further analyses. The organic content was decomposed using hydrogen peroxide (H$_2$O$_2$; concentration:
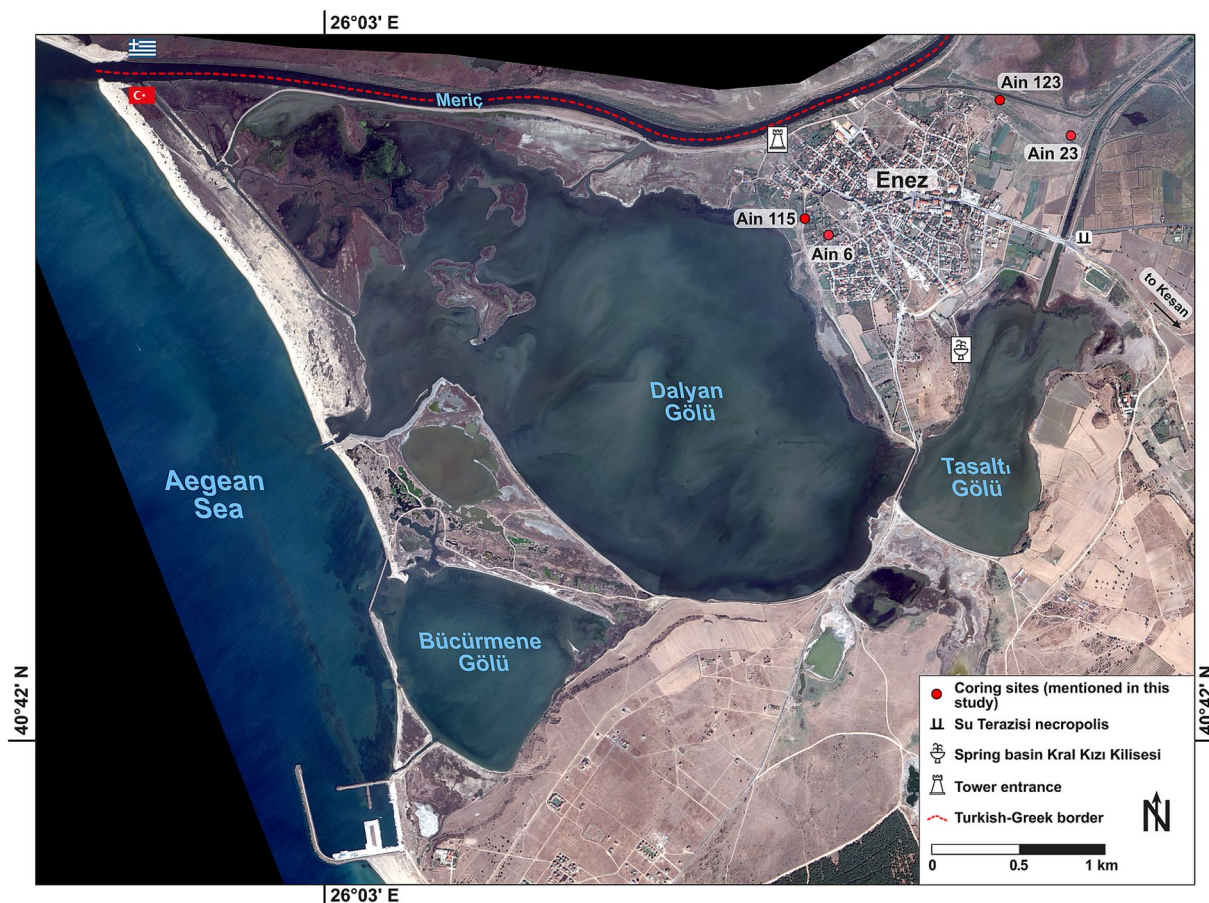
Figure 3. The coastal setting of Enez (Ainos). The locations of the corings presented in this study (Ain 6, 23, 115, and 123) are shown. Furthermore, the position of the used archeological sea-level limiting points is marked. Based on Worldview2; acquired 04th October 2012; composition of bands 1, 3, 6.

15%). Sodium pyrophosphate ($Na_4P_2O_7$; concentration: 47 g/l) was used as a dispersant before laser-based grain-size analyses were performed (*Beckman Coulter LS13320*). For the calculation of grain-size parameters after Folk and Ward (1957), the *GRADISTAT* software (Blott and Pye, 2001) was applied.

Up to 30 elements were determined using a portable XRF spectrometer (*Niton XL3t 980*). To ensure comparability of all XRF data and to reduce grain-size dependencies, each sample was ground to powder in a ball mill (*Retsch PM 400*) and subsequently pressed to pills before being measured (Ginau et al., 2018, 2020; Seeliger et al., 2018; Vött et al., 2011).

Due to the significant amount of XRF data, a Principal-Component Analysis (PCA) was performed using the *SPSS 25* software package to isolate the most important independent factors. The Kaiser–Meyer–Olkin measure of sampling adequacy was 0.779, representing a good factor analysis, and Bartlett's Test of Sphericity was significant ($p < 0.000$), indicating that correlations between parameters were robust enough for a PCA. Only factors with eigenvalues of $\geqslant 1$ were taken into consideration (Guttman, 1954; Kaiser, 1960). Examination of Kaiser's criteria and the scree plot yielded empirical justification for retaining two factors with eigenvalues exceeding 1 that accounted for 90.891 of the total variance. Among the factor solutions, the varimax-rotated two-factor solution yielded the most interpretable one, and most parameters loaded highly on only one of the two factors.

Foraminifers and ostracods were prepared by wet-sieving 1 cm³ samples through a 100 μm mesh to concentrate foraminiferal tests. At least 300 individual tests were subsequently picked from the retained sediment, under a stereoscopic microscope. For samples in which there were <300 specimens, all tests and valves were picked. Species were identified according to Cimerman and

Langer (1991) and Meriç et al. (2004) for foraminifera, and following Bonaduce et al. (1975) and Joachim and Langer (2008) for ostracoda.

Dating

The chronological framework of the cores is based on ^{14}C-AMS age estimates. ^{14}C-AMS dating was done at the Centre for Applied Isotope Studies, University of Georgia, Athens, USA (lab code: UGAMS) and the Beta Analytic Inc. Laboratory, Miami, USA (lab code: BETA). When possible, we used soft charcoal that is not prone to reworking. Otherwise, we bulk-sampled about 50 foraminiferal tests of the genus Ammonia for dating. Depending on the $\delta^{13}C$ value, each sample was calibrated using either the IntCal20 or the MARINE20 calibration curves of the recent Calib 8.20 (http://calib.org/calib) software (Reimer et al., 2020) with a marine reservoir effect of 390 ± 85 years and a ΔR of 35 ± 70 years (Siani et al., 2000). The latter used marine shells of known age sampled on the Dardanelles' shores and later stored in the Muséum national d'Histoire naturelle (Paris) to calculate the local marine reservoir age and its ΔR. However, because the spatio-temporal variation of the marine reservoir effect for the Aegean Sea – as well as worldwide – is still not fully understood, the ^{14}C-ages of marine carbonates should be interpreted carefully. Ages are reported in cal yrs BP (calibrated years before present; present = AD 1950) using a 2σ-confidence interval (Table 1).

Sea-level indicators

Sea-level index point based on Seeliger et al. Seeliger et al. (2017) present a novel approach to determine the position of former

Table 1. Radiocarbon datasheet. ^{14}C-AMS dating was carried out at Centre for Applied Isotope Studies, University of Georgia, Athens, USA (lab code: UGAMS) and the Beta Analytic Inc. Laboratory, Miami, USA (lab code: BETA). All ages were calibrated with the IntCal20 or Marine20 calibration curves depending on sample δ^{13}C using the recent Calib 8.20 software (Reimer et al., 2020). A marine reservoir effect of 390 ± 85 years and a ΔR of 35 ± 70 years (Siani et al., 2000) were applied. The calibrated ages are presented in calendar years BP with a 2σ confidence interval.

Sample code	Lab code	Material	Depth b.s.	Depth b.s.l.	d^{13}C (‰)	Libby age	Calibrated ^{14}C ages cal BP (2σ)
Ain 6|29	UGAMS-13086	Piece of charcoal	5.70 m	4.32 m	−14.4	4270 ± 25	4824–4867 BP
Ain 115|553	BETA-501448	Bulk sample of foraminifera	5.53 m	4.94 m	0.8	5890 ± 30	5873–6280 BP
Ain 123|179	BETA-499983	Piece of charcoal	1.79 m	1.68 m	−27.1	1840 ± 30	1637–1826 BP
Ain 123|413	BETA-501446	Bulk sample of foraminifera	4.13 m	4.02 m	2.1	4430 ± 30	4090–4605 BP

Depth b.s.: depth of the sample below the surface in m; Depth b.s.l.: depth of the sample below present-day mean sea level; δ^{13}C (‰): delta ^{13}C value in per mil; Libby age: uncalibrated age (in years) delivered by the respective laboratory; Calibrated ^{14}C ages BP (2σ): calibrated ages in calendar years BP (before AD 1950) with 2σ confidence interval.
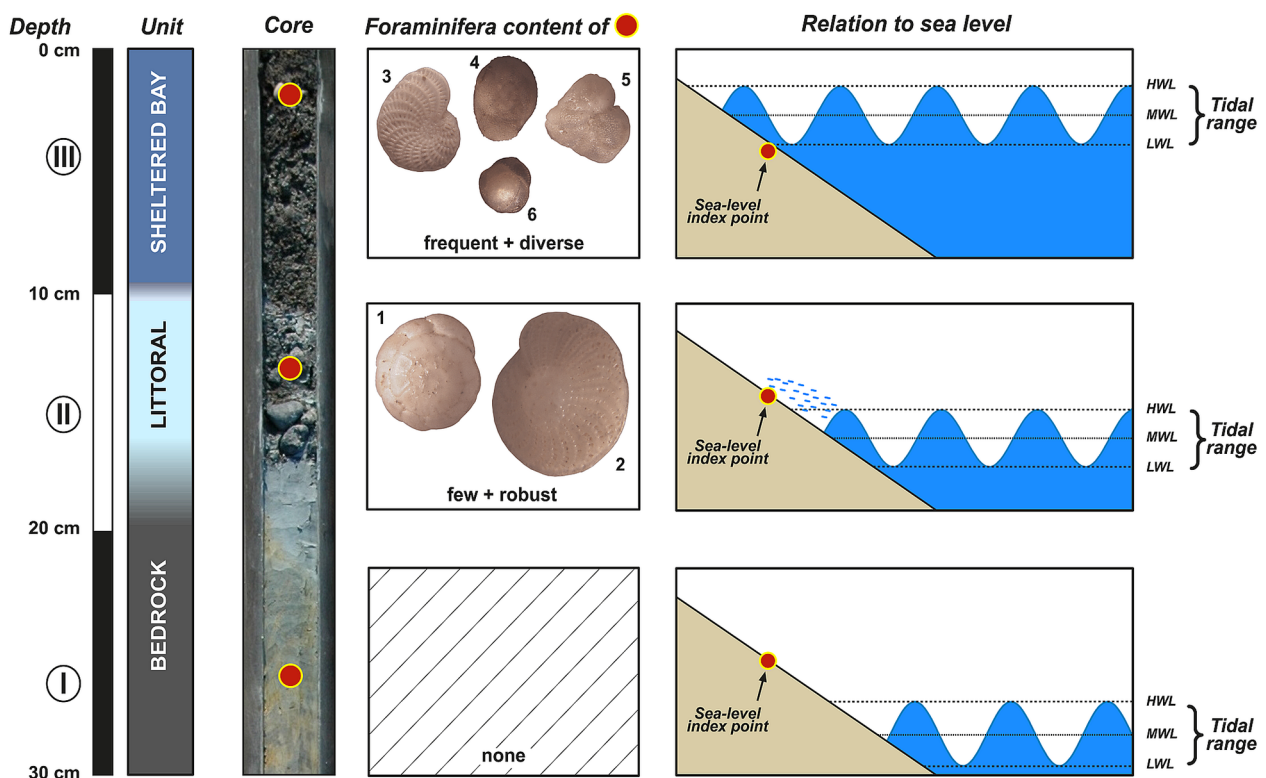

Figure 4. Foraminifera association in the context of the transgressive contact. (I) Before the onset of transgression. (II) The littoral facies with foraminifera *Ammonia compacta* (1) and *Elphidium crispum* (2). (III) Beginning of the shallow marine facies with *Elphidium complanatum* (3), *Rosalina globularis* (4), *Lobatula lobatula* (5), and *Asterigerinata mamilla* (6). The lowermost sample with characteristics of (III) was radiocarbon dated to gain the age of this sea-level index point. As the presented foraminifera are benthic species, the indicative meaning (e.g. the quantitative relationship between the sample and the present-day mean sea level (Shennan et al., 2018) ranges from the mean low water (LWL) to the mean high water (HWL).
HWL: high-water level; MWL: mean-water level; LWL: low-water level.

relative sea levels in sediment cores with transgressive contacts above bedrock, based on foraminiferal associations (Figure 4). The first occurrence of foraminifera in the sediments – for example, *Ammonia compacta* and *Elphidium crispum* – deposited during the Holocene marine transgression shows very robust species able to withstand the high-energy environment (Figure 4, unit II). Due to wash effects in the surf zone, they are transported to the lowermost part of the supratidal zone, directly above mean-sea level. Sea-level rise completely drowned the investigated site, attested by a shallow-marine association of foraminifera (*Rosalina globularis, Elphidium complanatum, Asterigerinata mamilla*, and *Lobatula lobatula*). The first occurrence of this association in the stratigraphy acts as a reliable sea-level indicator. Since the presented foraminifera are benthic species, the indicative meaning – that is, the quantitative relationship between the sample and the contemporary

mean sea level (Shennan et al., 2018) – ranges from the mean low water (LWL) to the mean high water (HWL) (Figure 4, unit III).

Since the sampling location is close to the bedrock, sediment compaction for this type of sea-level indicator is minor. This study adopted this approach and used charcoal and foraminifera for radiocarbon dating (Table 1).

Archeological sea-level limiting points. Furthermore, several archeological discoveries provide information about sea-level variations (Auriemma and Solinas, 2009; Khan et al., 2015, 2019; Vacchi et al., 2016, 2020; Figure 3). Judging by their chronology and function in Enez, these are: (1) a necropolis outside the ancient city walls; (2) a spring tapping inside a Byzantine church (Kral Kızı Kilisesi); and (3) the entrance level of a Late Byzantine fortification tower.

Su Terazisi necropolis. To the east of Enez, where the modern road to Keşan exits the city, the so-called "Su Terazisi" ("Water-Terrace") necropolis has been excavated (Figure 3). It includes inhumation and incineration graves of different types covering the whole period from the Greek-Archaic period to Late Antiquity. The remains of the oldest unearthed sarcophagi are of Archaic-Classical age (2650–2550 BP; seventh century BC). The base level of the deepest one was 0.5 m b.s.l. Initially, they were definitely placed on solid ground above sea level (we assume at least 1 m above the former sea level). Their position acts as a maximum limiting point of the Archaic-Classical sea level of in sum 1.5 m b.s.l. The sarcophagi from younger eras are situated above the present-day sea level and do not refine the RSL history.

Spring tapping inside a Byzantine church (Kral Kızı Kilisesi). Inside the Kral Kızı Kilisesi constructed on the western shore of the Taşaltı lagoon, two fresh-water spring basins were found used for religious purposes (Figure 3). The lowest point of the lower basin is 0.69 m b.s.l. It is assumed that these tappings were constructed above the former relative sea level to avoid the water turning brackish. Auriemma and Solinas (2009) discussed the indicative meaning of wells similar to these but stated that this is site-dependent. Therefore, we use the spring at Enez as an approximation that sea level was below that height. The age of the basin is constrained to older than 750 BP (AD 1200).

The entrance of a Late Byzantine tower in the northwest of modern Enez. In the northwest of Enez, directly at the Meriç River's southernmost branch, the ruins of a 10.7 m × 8.6 m large tower are located. Having been constructed on a bedrock outcrop, it is still standing, with two remaining floors; it is, however, in a degraded condition. The building technique and spolia of Late Byzantine age (600–500 BP; 1350–1450 AD) date the tower. Its entrance to the north is well preserved and leveled 0.25 m a.s.l. Auriemma and Solinas (2009) and Antonioli et al. (2007) stated a general value of about 0.6 m above former relative sea level for this type of public buildings, which fits our assumptions for Enez of 0.5–1 m. In sum, we can state a relative sea level of at least 0.25–0.75 m b.s.l. for the Late Byzantine period.

GIA modeling

To estimate the expected variation of RSL in the study area, we simulated the Glacial Isostatic Adjustment (GIA) process in response to the melting of the Late-Pleistocene ice sheets, based on global models currently available in the literature. In particular, we used the GIA models ICE-6G(VM5a) by Peltier et al. (2015) and the one developed at the Australian National University by Kurt Lambeck and collaborators (see, e.g. Lambeck et al., 2003; Nakada and Lambeck, 1987), hereafter referred to as ANU. The ice-time history of these three GIA models was implemented in the Sea-Level Equation solver SELEN4 (Spada and Melini, 2019), which has been solved on a global grid to maximum harmonic degree Lmax = 256. For the ICE model, we adopted the viscosity profile given by the author, while for ANU we employed a lithospheric thickness of 90 km, an upper-mantle and lower-mantle viscosity of 0.5×10^{21} Pa s and of 10^{22} Pa s, respectively, according to the range of parameters provided in Lambeck et al. (2017). In our modeling, we account for Earth-rotational variations, the migration of the shorelines in response to sea-level rise, and the transition from grounded to floating ice. For details, see Melini and Spada (2019) as well as Spada and Melini (2019) and the related Supplemental Material.

Results

As all three selected corings present similar sedimentological units, Ain 123 was selected as a case example (Figures 3 and 5).

Results of core Ain 123

Ain 123 (26°05′22.67″E; 40°43′45.80″N; final depth: 5 m b.s.; elevation: 0.11 m a.s.l.; Figures 3 and 5) is situated in the very north of Enez, close to the adjacent swampy-marsh area. Based on the microfaunal associations and the sedimentological results, the profile was divided into five (I–V) units (Figure 5).

The lowermost unit I – pre-Holocene, weathered limestone – was encountered at 4.22 m b.s. (4.11 m b.s.l.).

The overlying unit II extends up to 3.97 m b.s. (3.86 m b.s.l.) and consists of dark gray, well-sorted sands (mean 396–526 μm). PCA factor 1 (PCA F1), which represents the terrestrial influence based on Ti, Rb, Al, Fe, and Pb loadings, shows the lowest values of the entire profile (supplemental Appendix A1). Unit II is interspersed with relatively large pebbles (<3 cm) and some marine-shell debris. The foraminiferal suite comprises *Elphidium aculeatum, Ammonia parkinsoniana*, and *Quinqueloculina* spp., while *Cyprideis torosa, Aurila* sp., and *Semicytherura* spp. are the most abundant ostracod species. This unit is dated by a set of foraminifera at 4.13 m b.s. (4.02 m b.s.l.) to 4090–4605 cal yrs BP (Ain 123|413; Table 1).

Unit III extends to 2.45 m b.s. (2.34 m b.s.l.) and consists of dark gray sands (mean 428–850 μm) and is rich in organic micro-remains (mostly charcoal, shell fragments, and seagrass) as well as small pebbles (<1 cm). Toward the upper limit, a pebble cluster is noted. The values of PCA F1 are steadily rising. The foraminifera association is diverse and comprises mostly *Ammonia tepida, Ammonia parkinsoniana, Quinqueloculina* spp., and *Ammonia beccarii*, while just a few ostracod tests are present (*Propontocypris* sp., *Loxoconcha* sp., *Pontocythere turbida*, and *Leptocythere* spp.).

Above the pebble layer, unit IV starts at 2.45 m b.s. (2.34 m b.s.l.) and extends up to 1.30 m b.s. (1.19 b.s.l.). Unit IV is made of homogeneous fine gray silts (mean 13–93 μm) and shows lenses of clay and organic material in random order. PCA F1 is still steadily rising in this unit. The foraminifer association is not as diverse as in unit III. It comprises mostly *Ammonia tepida, Haynesina germanica, Ammonia parkinsoniana*, while the ostracod association is dominated by *Cyprideis torosa* associated with just a few specimens *Loxoconcha elliptica* and *Aurila* sp. A charcoal piece dates unit IV to 1637–1826 cal yrs BP (Ain 123|179 at 1.79 m b.s., 1.68 m b.s.l.).

Unit V is the topmost unit, developed between 1.30 m b.s. (1.19 m a.s.l.) and the present surface. It comprises poorly sorted, fine-grained brown silts and loams (mean 11–23 μm) with small pebbles (<0.5 cm), small fragments of charcoal, and plant remains. PCA F1 attains maximum values in this unit. Moreover, unit V does not contain foraminifera or ostracods, and farming activities mark the uppermost 0.34 m (plow horizon).

Discussion and interpretation

Combining the sedimentological and microfaunal findings helps to refine the results of Brückner et al. (2015) in characterizing the paleoenvironmental conditions in the surroundings of modern Enez. The present study provides new insights into the relative sea-level evolution of this area combined with the geochronological results.

Interpretation of core Ain 123 and a summary of the paleogeographic evolution of the area

The bedrock (Neogene limestone, unit I) outcrops on parts of the hill on which the Enez castle was built. This limestone was used at the regional scale as a building material. Consequently, its weathered part was encountered at the location of Ain 123 (Figure 5) at 4.22 m b.s. (4.11 m b.s.l.).

The transgressive, littoral unit II represents the onset of the Holocene sea-level rise at this site, tops unit I. Many pebbles, the
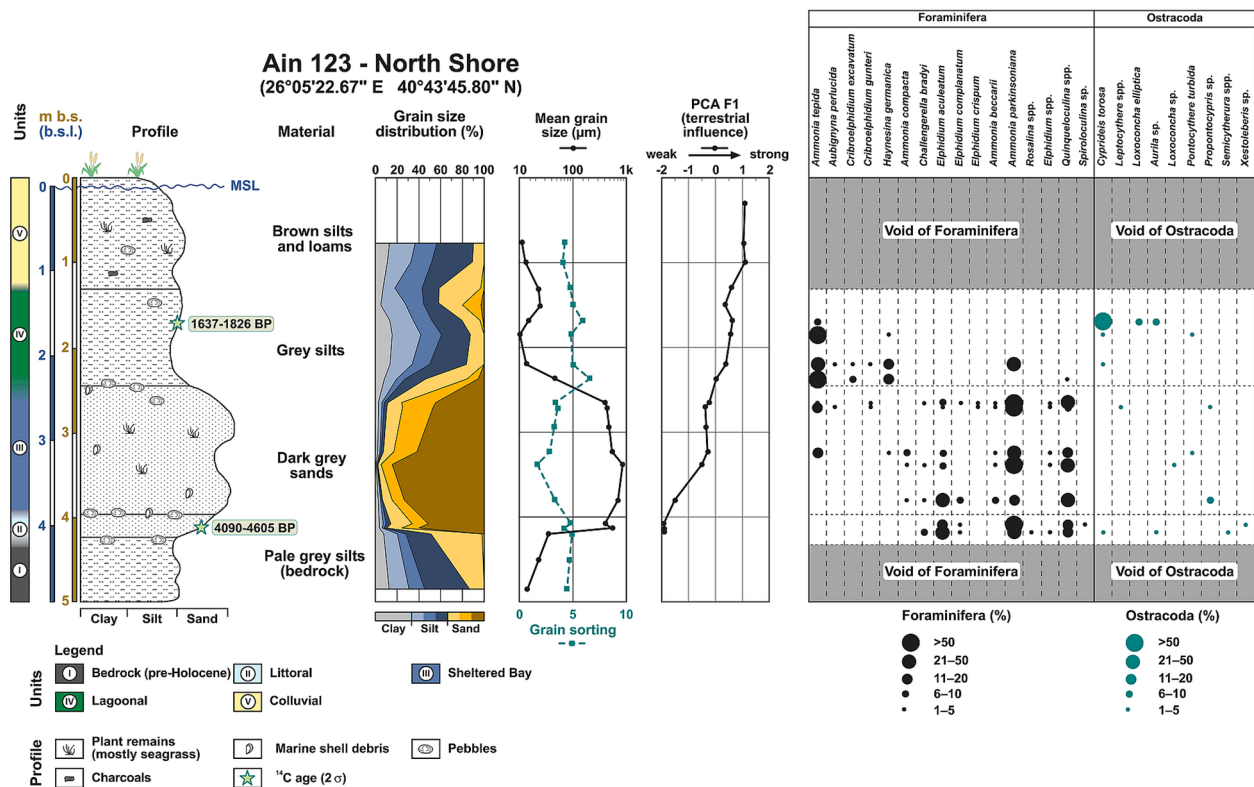
Figure 5. Sedimentary units, geochemical and microfaunal records of core Ain 123 at the northern shore of Enez (for location, see Figure 3). The abundance of ostracoda and foraminifera is given semi-quantitatively. The PCA F1 curve is based on the elements Ti, Rb, Al, Fe, and Pb reflecting terrestrial processes (see supplemental Appendix A1).

m b.s.: meter below present surface; m b.s.l.: meter below present-day mean sea level; MSL: present-day mean sea level.

coarse grain size, the poor sorting, and minimum PCA F1, which points to low terrestrial influence, attest to the high-energy nature of this environment. The low biodiversity and the sole occurrence of robust foraminifera, such as *Ammonia* spp. and *Elphidium* spp. in the lower part of unit II, indicate the high stress level of this littoral environment that is too energetic for most species. Following the dating results of Ain 123|413 (4090–4605 cal yrs BP; Table 1), the Holocene transgression had already reached this area during the second half of the 5th millennium BP.

Ongoing relative sea-level rise led to the formation of a shallow-water body represented by unit III. The greater water depth caused by the shoreline's inland migration led to reduced wave action at the core site, attested by good sorting. Besides, the high microfaunal diversity is consistent with a shallow-marine water body.

Due to the Meriç Delta's progradation, the area was later separated from the sea and transformed into a lagoonal environment (unit IV), comparable to core Ain 23 just east of coring site Ain 123 (see Brückner et al., 2015). The fine grain size, the poor sorting, the increasing terrestrial influence (PCA F1), and the decrease in microfauna species diversity are typical of lagoonal environments. These environmental changes started around a similar time to Ain 23, as shown for the Late Roman period by the core Ain 123|179 (1637–1826 cal yrs BP). This area was gradually silted up by high sediment supply from the Meriç, including human impact on sediment budgets. By Late Antiquity, the area had become marshland (unit V). This is supported by the disappearance of microfauna and the peak of PCA F1, consistent with terrestrial influence.

Sea-level index point from Ain 123

Following the approach described by Seeliger et al. (2017), the first occurrence of a fully established shallow-marine association of foraminifera (*Elphidium aculeatum, Elphidium complanatum,*

Rosalina spp., *Ammonia parkinsoniana*, and *Quinqueloculina* spp.) occurred at 4.13 m b.s. (4.02 m b.s.l.). A bulk sample of foraminifera from this depth was dated to 4090–4605 cal yrs BP (Ain 123|413; Table 1) and constituted our first sea-level index point.

An RSL curve for the Meriç delta

Using the aforementioned sea-level indicator, we created an RSL-curve based on three index points for the Meriç-delta region (Figure 6). Each coring (Ain 6, 115, and 123) furnished one index point, that is, the Holocene transgression's onset at the specific site (Figure 2). The curve starts with an index point at a depth of 4.94 m b.s.l. and ~6000 years ago (5873–6280 cal yrs BP; Ain 115|553 in Table 1). Rising rates are 0.6 mm/year until the next index point at a depth of 4.32 m b.s.l., ~4850 years ago (4824–4867 cal yrs BP; Ain 6|29 in Table 1) is reached. Due to the broad age range of the uppermost index point at 4.02 m b.s.l. ca. 4300 yrs ago (4090–4605 cal yrs BP; Ain 123|413 in Tab. 1), the gradient increases to 1.1 mm/yr. Unfortunately, no younger ages were generated due to the limitations of the indicator itself. Therefore, the upper part of the curve was extrapolated to the present day, with average rising rates of 0.9 mm/yr. The three archaeological sea-level limiting points fit this overall trend within their error limits. Referring to the entire study period, sea level rose at an average of 0.81 mm/yr.

Comparison with other RSL data from the Aegean

In the northern Aegean Sea, further field-based RSL curves were established (Figure 7) by Syrides et al. (2009), Pavlopoulos et al. (2007, 2013), and Seeliger et al. (2017).

Fifty kilometers south-west of Enez, Syrides et al. (2009) reconstructed the RSL history of the Greek island of Samothraki (Figure 7, gray squares). Therefore, valves of *Cerastoderma glaucum* collected just above the transgressive contact in several corings
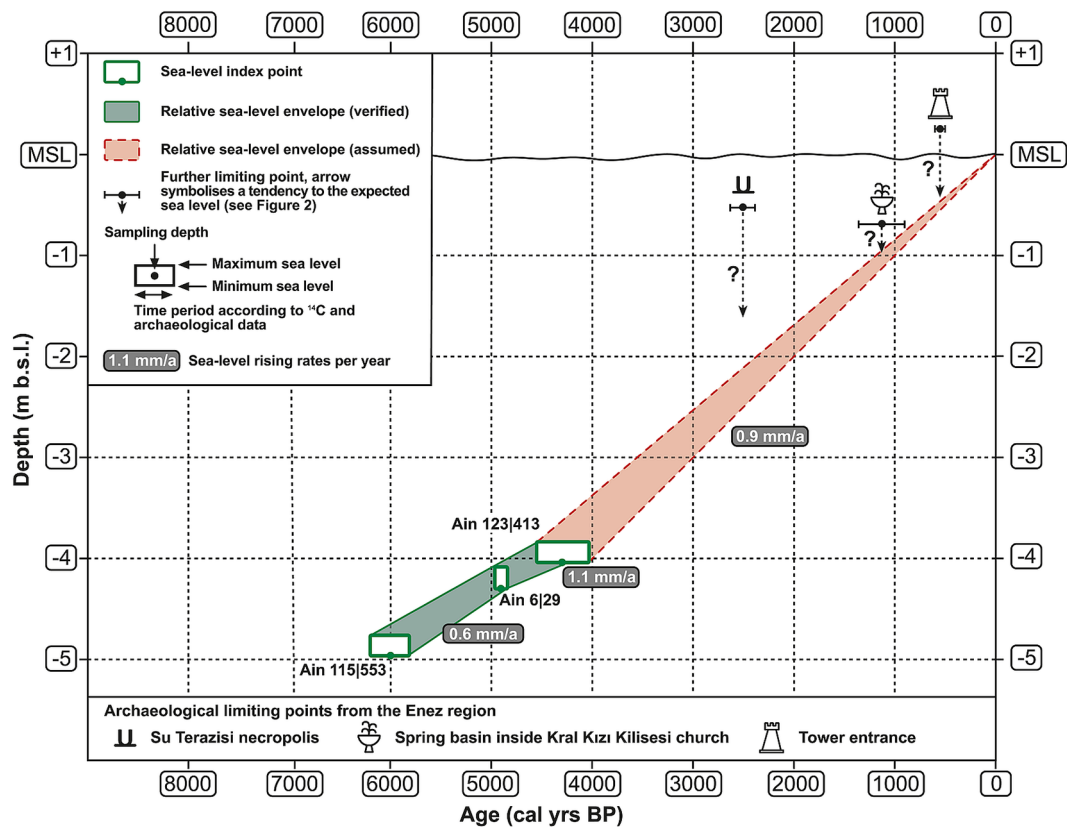
Figure 6. Relative sea-level (RSL) curve for the Meriç delta based on three sea-level index points following the approach of Seeliger et al. (2017) and the three archeological sea-level limiting points. The green envelope curve symbolizes the section with high sea-level estimation accuracy, while the red envelope curve shows an extrapolation until today.

(upward error bar of 0.5 m) were dated. These index points mesh nicely with our curve and provide insights into the RSL history before 7 ka BP. The combination of the Samothraki data and our index points shows a homogenous sea-level rise for the period 8–4.5 ka BP, and a backward extension of our curve is plausible.

Further south, on the island of Lemnos, Pavlopoulos et al. (2013) present an RSL curve for the region of the ancient city of Hephestia, which is tectonically active and often hit by earthquakes (ex. Figure 7, dashed black line). Because no morphological sea-level indicators exist above the present sea level, an absence of uplift is assumed. Based on the radiocarbon ages of mollusk shells (*Cerastoderma* sp.) and organic matter, the curve starts ~3900 cal yrs BP and is nearly identical to our curve with an average gradient of 0.79 mm/year.

The RSL curve published by Pavlopoulos et al. (2007) for the island of Skyros (Greece), a region with slight subsidence, is based on ^{14}C-dated peat and organic matter, supplemented by dated beachrock (ex. Figure 7, dashed pink line). The curves for Lemnos and Skyros are nicely correlated for the past 3750 years. A similar gradient, but with a vertical offset of approximately –0.5 m, hints at a more substantial subsidence rate, most probably caused by peat compaction (Marriner et al., 2012).

Finally, the curve described by Seeliger et al. (2017) for the Elaia region (Turkey) is the only curve with a similar temporal range as our curve (ex. Figure 7, dashed red line). Until approx. 4800 yrs BP, our curve is above that for Elaia. Beyond this date, and until present, it is below it. This could be due to the subsidence of the Bergama and Zeytindağ grabens (western Turkey) that, in the case of Elaia, is estimated to be ~1 mm/year (Aksu et al., 1987; Seeliger et al., 2013). Between 4500 yrs BP and today, both curves are broadly congruent, but it is important to stress that our curve has no data points for this time window. It is tenuous to state that the relative subsidence of the Meriç delta for the past 4500 yrs BP is

similar to the subsidence rates of the Bergama and Zeytindağ grabens (Seeliger et al., 2014, 2017). Nonetheless, our curve is in good agreement with all other regional curves for the last 4.5 ka.

Not only these RSL data underscore significant spatial variability in time-averaged rates of RSL change in the Aegean (Figure 8a), ranging from +4.6 mm/year at Epanomi to −5.4 mm/year at Chrisoskalitissa (Figure 8b). This significant spatial variability is the expression of highly vertical displacements caused by tectonic activity, sediment-isostasy, sediment compaction, and sediment budgets set against global eustatic changes and regional glacio-hydro-isostatic adjustments of the lithosphere. We generated three maps based on observed, predicted, and observed-predicted time-averaged rates of RSL change (Figures 9–11). Our analysis shows that tectonic uplift occurs along the Hellenic Arc's frontal margin (parts of Crete, Nisyros), in the northeast Aegean region (Thrace), and much of the central Aegean region. Sediment compaction and sediment loading play an essential role in the subsidence of areas in the northwest Aegean region (e.g. Enez, Thessaloniki Plain-Thermaikos Gulf). There is contrasting RSL evidence from Thessaloniki coastal plain with evidence for both regional uplift and subsidence. Finally, coastal sites in Turkey manifest opposite RSL trends due to the effects of tectonic fragmentation on vertical displacements (Figure 11).

Comparison with modeled sea-level curves for the study area

We calculated two models of RSL rise for the study area. All show a steady rise in RSL up to −0.5 m b.s.l. at ~6500 yrs BP. Following the ICE-6G (VM5a), RSL reached the present-day level ~5800 years ago and persisted at that level until today. The ANU model is in good agreement with ICE-6G (VM5a), showing a slower rate in RSL rise but reaching a maximum of ~+0.20 m
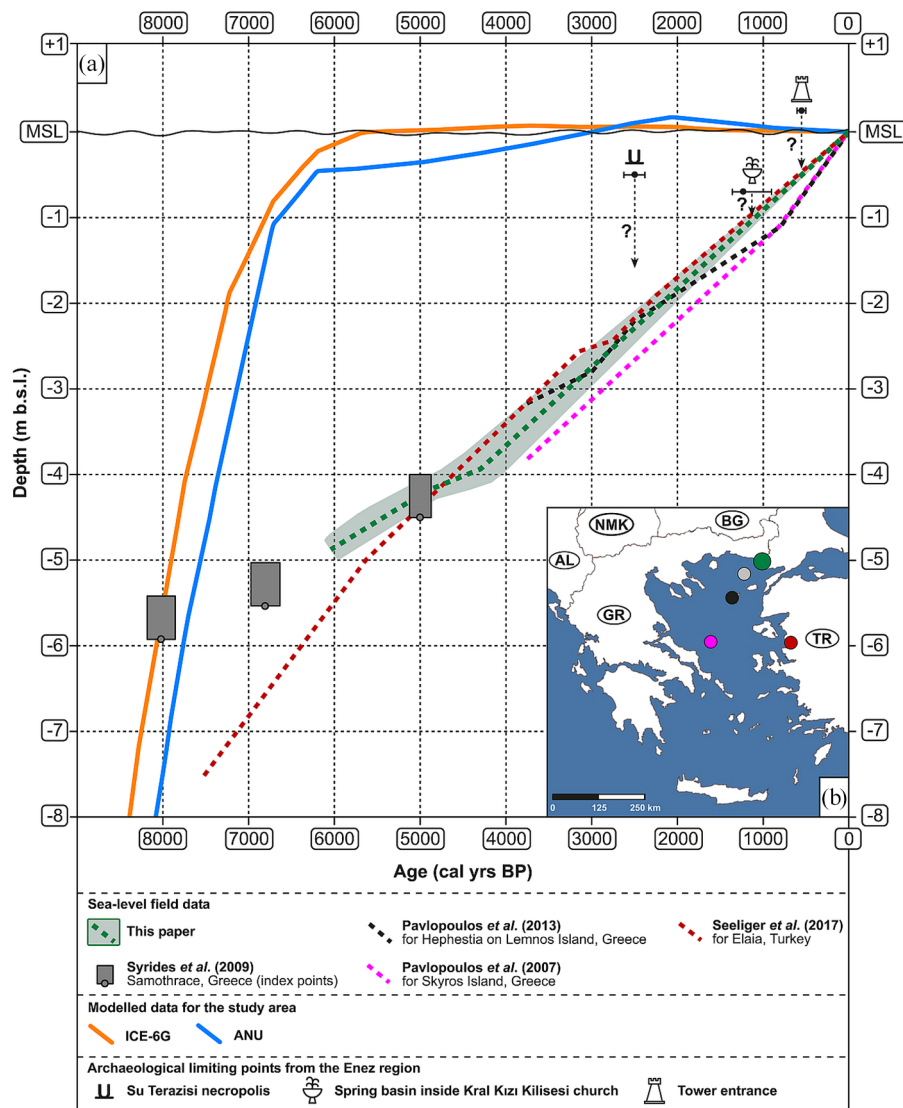
Figure 7. Modeled RSL curve for the area around Ainos compared with other curves for the northern Aegean region. (a) Selected RSL curves for sites in the Aegean Sea as well as the predicted GIA curves according to the two models described in section 3.5 ICE-6G (VM5a) and ANU for the sea area south of Enez. (b) Location of the study sites mentioned in Figure 7a in the Aegean region projected in Figure 2b. The same colors are used for each study site in Figure 7a and b.

above the present-day around 2000 yrs BP, when Ainos was densely settled. For the ANU model and ICE-6G (VM5a), constant relative sea-level variations for the past 3000 years can be stated. Interestingly, all modeled curves are above the level of the sarcophagi of Archaic age and the spring basin, which is, of course, in conflict with reality.

The reasons for this significant offset between the modeled curves and the field-based data points are manifold. The RSL predictions obtained by the two GIA models in Figure 7 reflect structural differences among them. These include the geometry of the ice complexes, their deglaciation chronology, the viscosity profile of the mantle, and the lithospheric thickness (Melini and Spada, 2019). The study area lies far from the major glaciation centers, such as the Fennoscandian Ice Sheet or the glaciated European Alps. Therefore, the ice equivalent meltwater (eustatic) factor is more important compared to the ice-induced component.

Furthermore, it is widely accepted that the world's deltas have subsided at various temporal and spatial scales (Syvitski et al., 2009) – a phenomenon mainly attributed to dewatering, compaction, oxidation of organic material, isostatic adjustment, and neotectonics. Within this context, tectonic subsidence of the Samothraki Plateau and adjacent areas is attested and attributed to sediment loading by the Nestos, Kompsatos, Lissos, and Meriç rivers

(Poulos and Kotinas, 2020; Figure 1). Furthermore, the nearby NAT also manifests high rates of subsidence at a regional scale. Based on the work of Perissoratis and Conispoliatis (2003) as well as Piper and Perissoratis (1991), the rate of subsidence on the Samothraki Plateau varies between 0.05 mm/year and 0.7 mm/year, with a spatially averaged subsidence rate for the Plateau of 0.3 mm/year.

Additionally, calculating a minimum value of subsidence using the sarcophagi basement back to the Seventh century BC (2650–2550 BP) is helpful in this context. The deepest basement was found at 0.5 m b.s.l. Assuming the water level was just below the basement (1 m b.s.l. for the calculation, which is unrealistic as the former settlers left more space between the sarcophagi and the water table), we can calculate a minimum rate of subsidence of ~0.3 mm/year and therefore neglect all rates below that number for further calculations. Using 0.3 mm/year for the period of interest results in 1.5 m (5000 years ago) and 1.8 m (6000 years ago) of subsidence. In contrast, using the maximum rate of 0.7 mm/year suggested by Piper and Perissoratis (1991) leads to a total amount of subsidence of 3.5 m (5000 years before today) and 4.2 m (6000 years before today). Therefore, most of the resulting differences between the field-based data and the modeled ones are due to the Samothraki Plateau subsidence.
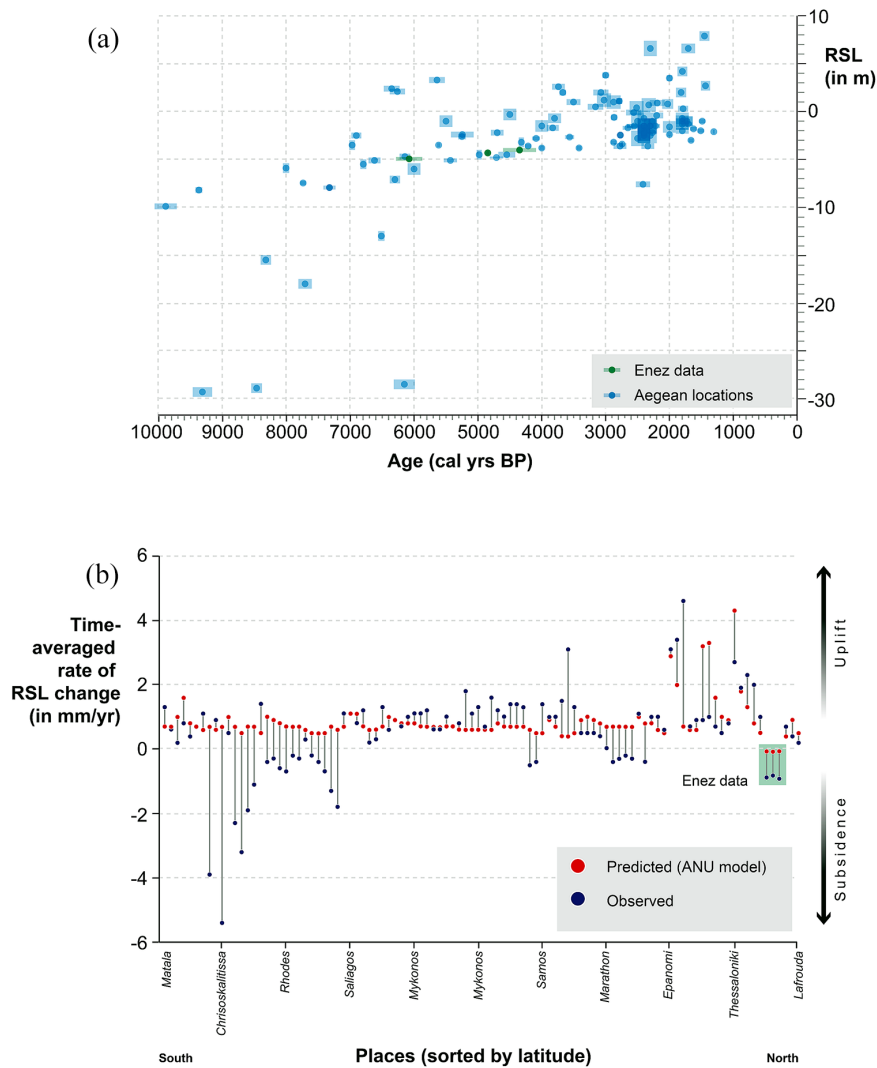
Figure 8. (a) Overview of all sea-level index points mentioned in this study. The three new ones from the Enez region are marked in green and fit well with the overall data cloud. (b) Comparison of the predicted and the observed heights for the locations of this study.
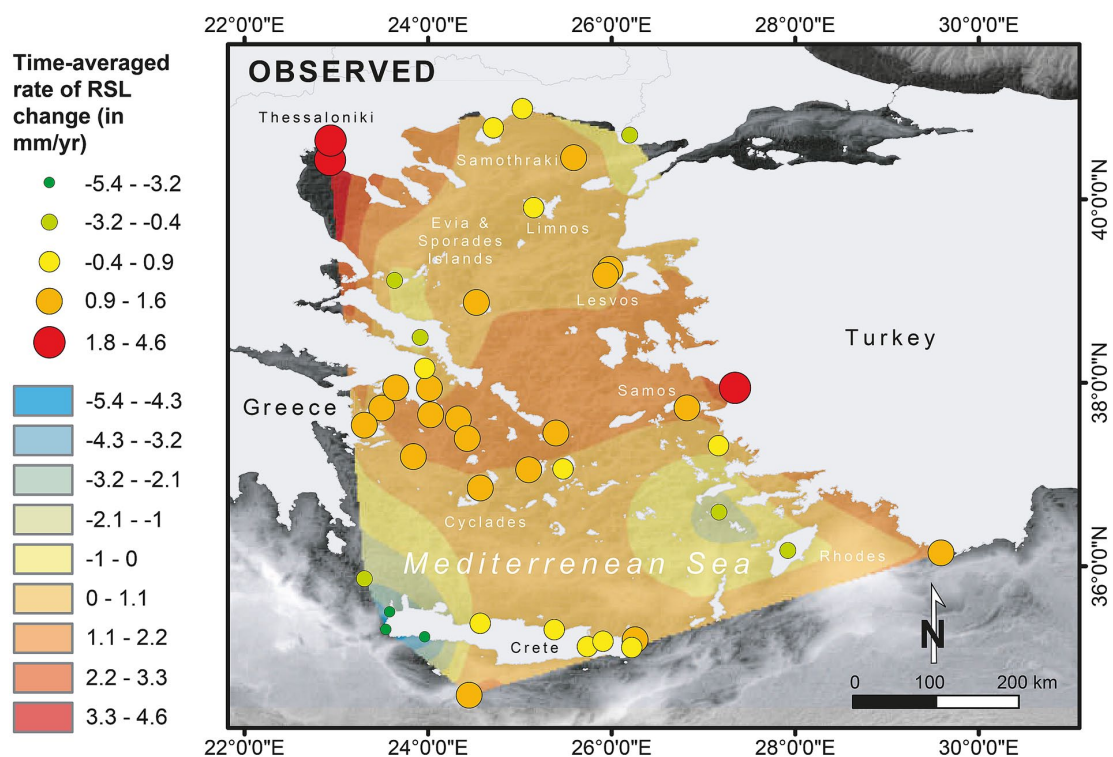

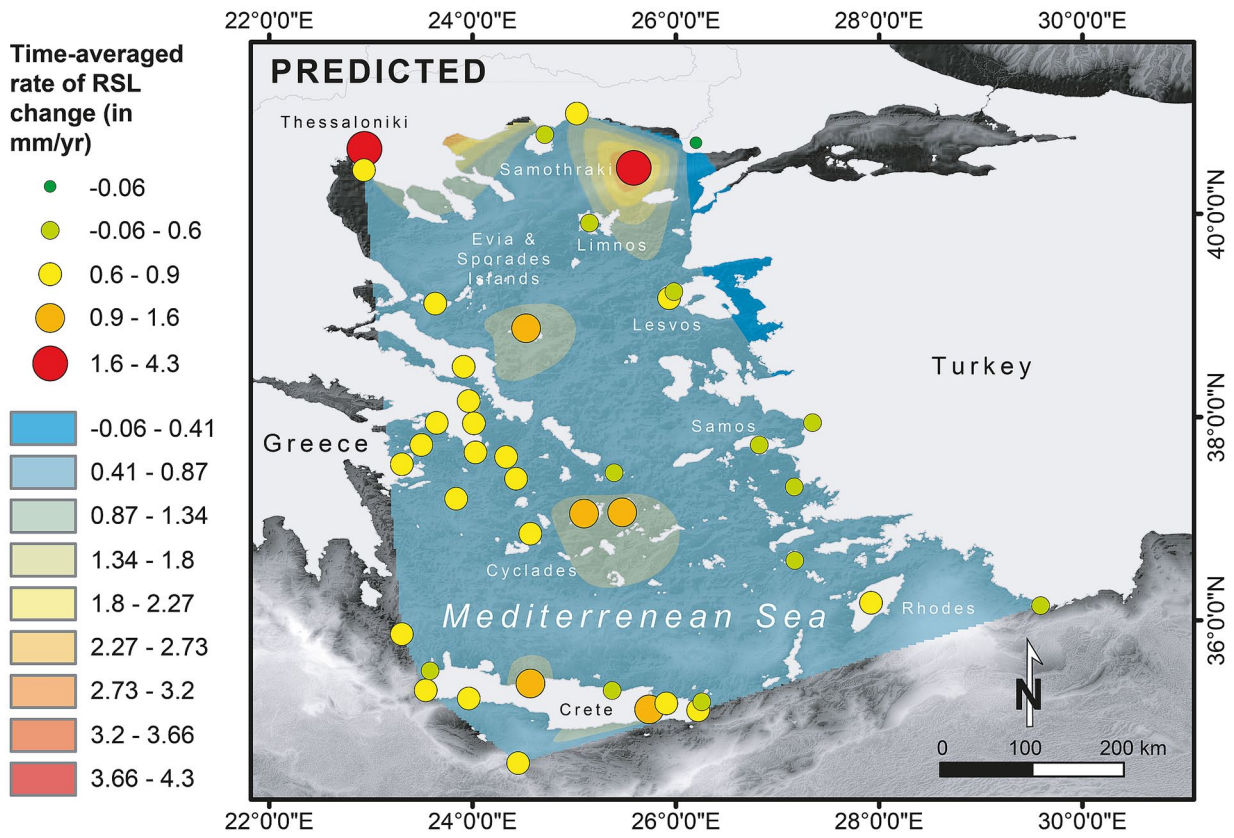**Figure 9.** Observed rates of RSL changes in the Aegean Region based on field data.

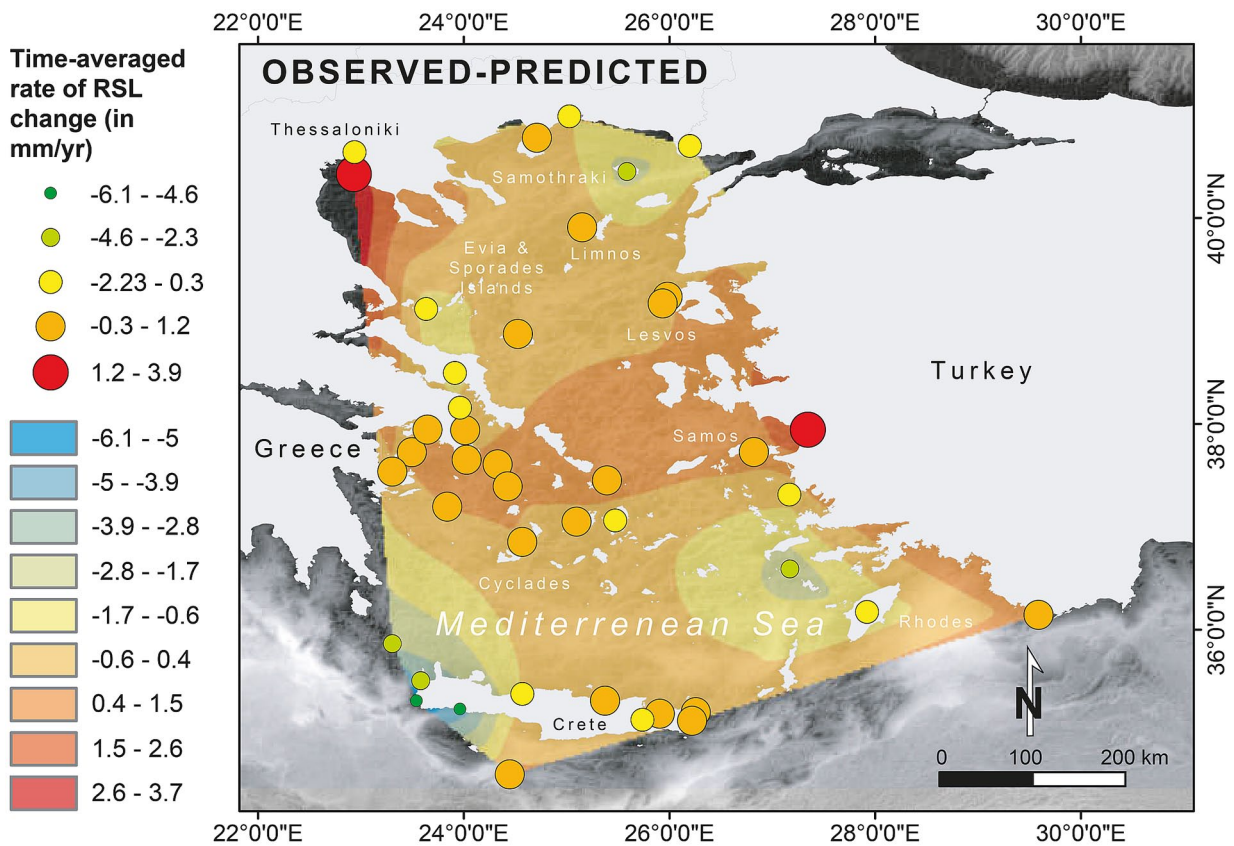**Figure 10.** Predicted rates of RSL change in the Aegean Region based on the ANU geophysical model.

Figure 11. Observed – predicted rates of RSL change in the Aegean Region. The ANU geophysical prediction data were subtracted from the field data points to assess the amplitude of land-level movements (tectonics, sediment compaction).

Conclusions

We applied the methodology of Seeliger et al. (2017) to the Meriç delta on the northern Aegean coast. The reconstructed RSL history meshes nicely with the areas of Samothraki (Syrides et al., 2009) and Elaia. We avoided problems of post-depositional compaction by using index points close to bedrock. Regressive phases were hard to identify using the Seeliger et al. (2017) methodology. Furthermore, the use of archeological sea-level limiting points (leveled sarcophagi, a spring basin, and the entrance of a tower) confirms that sea level is presently at its Holocene maximum. By comparing the curve with the predictions from the implementation of two GIA models, that is, ICE-6G(VM5a) and ANU, we conclude that most of the offset between the modeled and field-based data results from subsidence of the area of Ainos in connection with the Samothraki Plateau (sediment loading, dewatering, compaction, neotectonics). This does not explain all of the variations. Therefore, we argue that the models do not satisfactorily mirror the Holocene sea-level evolution of the northern Aegean region. This statement is supported by the fact that the RSL curves for other areas in the region – the islands of Lemnos, Skyros, and Samothraki – fit well with our curve but do not match the modeled ones. Our data further confirm that none of the available geophysical models can resolve the GIA-related deformations in the Mediterranean in a comprehensive manner (Vacchi et al., 2018). The development of a Mediterranean transfer function based on micropaleontological assemblages may help to overcome this problem. In fact, an improved tuning of the GIA models is strongly dependent on the production of high-resolution sea-level data derived from low-energy coastal environments (e.g. Shaw et al., 2016). These proxies are notably lacking in much of the eastern Mediterranean basin, notably for the early to mid-Holocene. This is an exciting avenue for future RSL research in the area.

Author contributions

MS, AP, and PF designed this study. FS, KS, AD, HB, and MS performed the geoarchaeological fieldwork, mainly containing drilling, sediment sampling, and leveling the coring locations via DGPS. AP and MS carried out the laboratory analyses. NM, MV, and GS designed the study of the different GIA models and calculated the final plots. MS wrote the first draft of the manuscript that all co-authors later improved. MS created most of the figures. HB, TS, and AD acquired the funding for this research. SB acted as a valuable counterpart during the fieldwork and dated the sarcophagi unearthed in the necropolis due to his immense archaeological expertise. SB, AD, and TS provided the archaeological and historical data for this paper.

ORCID iDs

Martin Seeliger [ID] https://orcid.org/0000-0002-2584-1098
Anca Dan [ID] https://orcid.org/0000-0001-6468-9327

Supplemental material

Supplemental material for this article is available online.

Note

1. Abbreviations: RSL = relative sea level; DGPS = Differential Global Positioning System; LCS = local coordinate system; m b.s. = meters below the surface; m a.s.l. = meters above the present mean sea level; m b.s.l. = meters below the present mean sea level; XRF = X-ray fluorescence; cal yrs BP = calibrated years before present, present means 1950 after the birth of Christ (AD 1950), GIA = Glacial Isostatic Adjustment.

References

Aksu AE, Piper DJW and Konuk T (1987) Late Quaternary tectonic and sedimentary history of outer İzmir and Çandarlı Bays, Western Turkey. *Marine Geology* 76: 89–104.

Antonioli F, Anzidei M, Lambeck K et al. (2007) Sea level change during Holocene from Sardinia and northeastern Adriatic (central Mediterranean Sea) from archaeological and geomorphological data. *Quaternary Science Reviews* 26: 2463–2486.

Armijo R, Meyer B, Hubert A et al. (1999) Westward propagation of the North Anatolian Fault into the northern Aegean: Timing and kinematics. *Geology* 27: 267–270.

Auriemma R and Solinas E (2009) Archaeological remains as sea level change markers: A review. *Quaternary International* 206: 134–146.

Bartz M, Rixhon G, Kehl M et al. (2017) Unravelling fluvial deposition and pedogenesis in ephemeral stream deposits in the vicinity of the prehistoric rock shelter of Ifri n'Ammar (NE Morocco) during the last 100 ka. *Catena* 152: 115–134.

Barut IF, Nazik A, Balkıs N et al. (2015) Ostracoda as bioindicators of anthropogenic impact in salt lakes, saltpans, and a lagoon: A case study from the Gulf of Saros coast (NE Aegean Sea), Turkey. *Revue de Micropaléontologie* 58: 351–367.

Benjamin A, Rovere A, Fontana A et al. (2017) Late Quaternary sea-level changes and early human societies in the central and eastern Mediterranean Basin: An interdisciplinary review. *Quaternary International* 449: 29–57.

Blott SJ and Pye K (2001) GRADISTAT: A grain size distribution and statistics package for the analysis of unconsolidated sediments. *Earth Surface Processes and Landforms* 26: 1237–1248.

Bonaduce G, Ciampo G and Masoli M (1975) Distribution of Ostracoda in the Adriatic Sea. *Pubblicazioni della Stazione zoologica di Napoli* 40: 1–304.

Brückner H, Kelterbaum D, Marunchak O et al. (2010) The Holocene sea level story since 7500 BP – Lessons from the Eastern Mediterranean, the Black and the Azov Seas. *Quaternary International* 225(2): 160–179.

Brückner H, Müllenhoff M, Gehrels R et al. (2006) From archipelago to floodplain – geographical and ecological changes in Miletus and its environs during the last six millennia (Western Anatolia, Turkey). *Zeitschrift für Geomorphologie* 142: 63–83.

Brückner H, Schmidts TH, Bücherl H et al. (2015) Die Häfen und ufernahen Befestigungen von Ainos – eine Zwischenbilanz. In: Schmidts Th and Vučetić MM (eds) *Häfen*

im 1. Millennium AD: bauliche Konzepte, herrschaftliche und religiöse Einflüsse. Mainz: Römisch-Germanisches Museum, pp.53–76 (in German).

Cimerman F and Langer MR (1991) *Mediterranean Foraminifera*. Ljubljana: Slovenska Akademija Znanosti in Umetnosti, Academia Scientarium et Artium Slovenca.

EMODnet Bathymetry Consortium (2018) EMODnet Digital Bathymetry (DTM). http://doi.org/10.12770/18ff0d48-b203-4a65-94a9-5fd8b0ec35f6

Ernst W (1970) *Geochemical Facies Analysis*. Amsterdam, London, New York, NY: Elsevier.

Feuser S, Pirson F and Seeliger M (2018) The harbour zones of Elaia – the maritime city of Pergamum. In: Carnap-Bornheim C, Daim F, Ettel P et al. (eds) *Harbours as Objects of Interdisciplinary Research – Archaeology+History+Geosciences*. Mainz: Römisch-Germanisches Museum, pp.91–103.

Folk RL and Ward WC (1957) Brazos River bar: A study in the significance of grain size parameters. *Journal of Sedimentary Petrology* 27: 3–26.

Galanidou N, Dellaporta K and Sakellariou D (2020) Greece: Unstable landscapes and underwater archaeology. In: Bailey G, Galanidou N, Peeters H et al. (eds) *The Archaeology of Europe's Drowned Landscapes*. Cham: Springer, pp.371–392.

Ginau A, Schiestl R and Wunderlich J (2018) Integrative geoarchaeological research on settlement patterns in the dynamic landscape of the northwestern Nile delta. *Quaternary International* 511: 51–67.

Ginau A, Steiniger D, Hartmann R et al. (2020) What settlements leave behind — pXRF compositional data analysis of archaeological layers from Tell el-Fara'in (Buto, Egypt) using machine learning. *Palaeogeography, Palaeoclimatology, Palaeoecology* 546: 109666.

Guttman L (1954) Some necessary conditions for common-factor analysis. *Psychometrika* 19(2): 149–161.

Jackson J (1994) Active tectonics of the Aegean region. *Annual Review of Earth and Planetary Sciences* 22: 239–271.

Joachim F and Langer M (2008) *The 80 Most Common Ostracods from the Bay of Fetoveia, Elba Island (Mediterranean Sea)*. Bonn: Bonn University Publisher.

Kaiser HF (1960) The application of electronic computers to factor analysis. *Educational and Psychological Measurement* 20(1): 141–151.

Kayan İ (1988) Late-Holocene sea-level changes on the Western Anatolian coast. *Palaeogeography, Palaeoclimatology, Palaeoecology* 68(2–4): 205–218.

Khan NS, Ashe E, Horton B et al. (2017) Drivers of Holocene sea-level change in the Caribbean. *Quaternary Science Reviews* 155: 13–36.

Khan NS, Ashe E, Shaw TA et al. (2015) Holocene relative sea-level changes from near-, intermediate-, and far-field locations. *Current Climate Change Reports* 1(4): 247–262.

Khan NS, Horton BP, Engelhart S et al. (2019) Inception of a global atlas of sea levels since the last glacial maximum. *Quaternary Science Reviews* 220: 359–371.

Kraft JC, Kayan İ and Erol O (1980) Geomorphic reconstructions in the environs of ancient Troy. *Science* 209: 776–782.

Lambeck K and Purcell A (2005) Sea-level change in the Mediterranean Sea since the LGM: Model predictions for tectonically stable areas. *Quaternary Science Reviews* 24: 1969–1988.

Lambeck K, Purcell A, Johnston P et al. (2003) Water-load definition in the glacio-hydro-isostatic sea level equation. *Quaternary Science Reviews* 22(2): 309–318.

Lambeck K, Purcell A and Zhao S (2017) The North American Late Wisconsin ice sheet and mantle viscosity from glacial rebound analyses. *Quaternary Science Reviews* 158: 172–210.

Maravelis AG, Pantopoulos G, Tserolas P et al. (2015) Accretionary prism–forearc interactions as reflected in the sedimentary fill of southern Thrace Basin (Lemnos Island, NE Greece). *International Journal of Earth Sciences* 104: 1039–1060.

Marriner N, Flaux C, Morhange C et al. (2012) The Nile delta's sinking past: Quantifiable links with Holocene compaction and climate-driven changes in sediment supply? *Geology* 40: 1083–1086.

Melini D and Spada G (2019) Some remarks on glacial isostatic adjustment modelling uncertainties. *Geophysical Journal International* 218:401–413.

Meriç E, Avsar N and Bergin F (2004) Benthic foraminifera of eastern Aegean Sea (Turkey) systematics and autoecology. *Turkish Marine Research Foundation* 18: 1–306.

Nakada M and Lambeck K (1987) Glacial rebound and relative sea level variations: a new appraisal. *Geophysical Journal International* 90(1): 171–224.

Papoulia C (2017) Seaward dispersals to the NE Mediterranean islands in the Pleistocene. The lithic evidence in retrospect. *Quaternary International* 431(B): 64–87.

Pavlopoulos K, Fouache E, Sidiropoulou M et al. (2013) Palaeoenvironmental evolution and sea-level changes in the coastal area of NE Lemnos Island (Greece) during the Holocene. *Quaternary International* 308–309: 80–88.

Pavlopoulos K, Triantaphyllou M, Karymbalis E et al. (2007) Landscape evolution recorded in the embayment of Palamari (Skyros Island, Greece) from the beginning of the Bronze Age until recent times. *Géomorphologie: Relief, Processus, Environnement* 13(1): 37–48.

Peltier WR, Argus DF and Drummond R (2015) Space geodesy constrains ice age terminal deglaciation: The global ICE-6G C (VM5a) model. *Journal of Geophysical Research: Solid Earth* 120(1): 450–487.

Perissoratis C and Conispoliatis N (2003) The impacts of sea-level changes during latest Pleistocene and Holocene times on the morphology of the Ionian and Aegean seas (SE Alpine Europe). *Marine Geology* 196: 145–156.

Pint A, Seeliger M, Frenzel P et al. (2015) The environs of Elaia's ancient open harbor–a reconstruction based on microfaunal evidence. *Journal of Archaeological Science* 54: 340–355.

Piper DJW and Perissoratis C (1991) Quaternary sedimentation on the north Aegean continental margin, Greece. *American Association of Petroleum Geologists* 75(1): 46–61.

Poulos S and Kotinas V (2020) Physio-geographical characteristics of the marine regions and their catchment areas of the Mediterranean Sea and Black Sea marine system. *Physical Geography*. Epub ahead of print 22 May 2020. DOI: 10.1080/02723646.2020.1762960.

Rabbel W, Wilken D, Wunderlich T et al. (2015) Geophysikalische Prospektion von Hafensituationen – Möglichkeiten, Anwendungen und Forschungsbedarf. In: Schmidts Th and Vučetić MM (eds) *Häfen im 1. Millennium AD: bauliche Konzepte, herrschaftliche und religiöse Einflüsse*. Mainz: Römisch-Germanisches Museum, pp. 329–340 (in German).

Reimer PJ, Austin WEN, Bard E et al. (2020) The INTCAL20 Northern Hemisphere radiocarbon age calibration curve (0–55 cal kBP). *Radiocarbon* 62(4): 725–757.

Sakellariou D and Galanidou N (2015) Pleistocene submerged landscapes and Palaeolithic archaeology in the tectonically active Aegean region. In: Harff J, Bailey G and Lüth F (eds) *Geology and Archaeology: Submerged Landscapes of the Continental Shelf*, vol. 411. London: Geological Society Special Publications, pp.145–178.

Saltogianni V, Gianniou M, Moschas F et al. (2016) Pattern of dynamic displacements in a strike-slip earthquake. *Geophysical Research Letters* 43(13): 1–8.

Schwardt M, Köhn D, Wunderlich T et al. (2020) Characterization of silty to fine-sandy sediments with SH waves full

waveform inversion in comparison with other geophysical methods. *Near Surface Geophysics* 18(3): 217–248.

Seeliger M, Bartz M, Erkul E et al. (2013) Taken from the sea, reclaimed by the sea: The fate of the closed harbour of Elaia, the maritime satellite city of Pergamum (Turkey). *Quaternary International* 312: 70–83.

Seeliger M, Brill D, Feuser S et al. (2014) Purpose and age of underwater walls in the Bay of Elaia (western Turkey)–a multidisciplinary approach. *Geoarchaeology* 29: 138–155.

Seeliger M, Pint A, Frenzel P et al. (2017) Foraminifera as markers of Holocene sea-level fluctuations and water depths of ancient harbours—a case study from the Bay of Elaia (W Turkey). *Palaeogeography, Palaeoclimatology, Palaeoecology* 482: 17–29.

Seeliger M, Pint A, Feuser S et al. (2019) Elaia, Pergamon's maritime satellite: The rise and fall of an ancient Harbour city shaped by shoreline migration. *Journal of Quaternary Science* 34(3): 228–244.

Seeliger M, Pint A, Frenzel P et al. (2018) Using a multi-proxy approach to detect and date a buried part of the Hellenistic city wall of Ainos (NW Turkey). *Geosciences* 8: 357.

Shaw TA, Kirby JR, Holgate S et al. (2016) Contemporary salt-marsh foraminiferal distribution from the Adriatic coast of Croatia and its potential for sea-level studies. *The Journal of Foraminiferal Research* 46(3): 314–332.

Shennan I, Bradley SL and Edwards R (2018) Relative sea-level changes and crustal movements in Britain and Ireland since the Last Glacial Maximum. *Quaternary Science Reviews* 188: 143–159.

Siani G, Paterne M, Arnold M et al. (2000) Radiocarbon reservoir ages in the Mediterranean Sea and Black Sea. *Radiocarbon* 42: 271–280.

Spada G and Melini D (2019) SELEN4 (SELEN version 4.0): A Fortran program for solving the gravitationally and topographically self-consistent sea-level equation in glacial isostatic adjustment modeling. *Geoscientific Model Development* 12(12): 5055–5075.

Syrides G, Vouvalidis K, Albanakis K et al. (2009) Palaeogeographical evolution and sea level changes during Holocene in the prehistoric settlement of Mikro Vouni (Samothrace Island, Greece). *Zeitschrift für Geomorphologie* 53(1): 39–54.

Syvitski JPM, Kettner AJ, Overeem I et al. (2009) Sinking deltas due to human activities. *Nature Geoscience* 2(10): 681–686.

Theocharis A and Georgopoulos D (1993) Dense water formation over the Samothraki and Limnos Plateaux in the north Aegean Sea (Eastern Mediterranean Sea). *Continental Shelf Research* 13(8–9): 919–939.

Uckac S, Garcia-Gorriz E and Stips A (2006) *General Estuarine Transport Model (GETM) Validation by Using In-situ Measurements and Remote Sensing Data in the Aegean Sea*. Luxemburg: Office for Official Publications of the European Communities.

Vacchi M, Ermolli ER, Morhange C et al. (2020). Millennial variability of rates of sea-level rise in the ancient harbour of Naples (Italy, western Mediterranean Sea). *Quaternary Research* 93(1): 284–298.

Vacchi M, Ghilardi M, Melis RT et al. (2018) New relative sea-level insights into the isostatic history of the Western Mediterranean. *Quaternary Science Reviews* 201: 396–408.

Vacchi M, Marriner N, Morhange C et al. (2016) Multiproxy assessment of Holocene relative sea-level changes in the western Mediterranean: Sea-level variability and improvements in the definition of the isostatic signal. *Earth Science Reviews* 155: 172–197.

Vacchi M, Rovere A, Chatzipetros A et al. (2014) An updated database of Holocene relative sea-level changes in NE Aegean Sea. *Quaternary International* 328–329: 301–310.

Vacchi M, Rovere A, Zouros N et al. (2012) Spatial distribution of sea-level markers on Lesvos Island (NE Aegean Sea): Evidence of differential relative sea-level changes and the neotectonic implications. *Geomorphology* 159–160: 50–62.

Vött A, Bareth G, Brückner H et al. (2011) Olympia's harbour site Pheia (Elis, Western Peloponnese, Greece) destroyed by tsunami impact. *Die Erde* 142: 259–288.